Received: 1 July 2022 | Revised: 9 November 2022 | Accepted: 11 December 2022

DOI: 10.1111/ejss.13336

SPECIAL ISSUE PAPER

European Journal of Soil Science WILEY

Monitoring sedimentary areas from mine waste products with Sentinel-2 satellite images: A case study in the SE of Spain

Inés Pereira[1] | **Sara Alcalde-Aparicio**[2] | **Montserrat Ferrer-Julià**[1] | **María Francisca Carreño**[3] | **Eduardo García-Meléndez**[1]

[1]Biological and Environmental Sciences Faculty, University of León, Research Group on Environmental Geology, Quaternary and Geodiversity (Q-GEO), Leon, Spain

[2]Soil Science and Agricultural Chemistry Area, School of Agriculture Engineering, Department of Agricultural Science and Engineering, University of León, Research Group on Environmental Geology, Quaternary and Geodiversity (Q-GEO), Leon, Spain

[3]Geological-Mining Technological Unit, Centro del Mármol y Piedra y Materiales (CTM), Cehegín, Spain

Correspondence
Inés Pereira, Biological and Environmental Sciences Faculty, University of León, Research Group on Environmental Geology, Quaternary and Geodiversity (Q-GEO), Leon, 24071, Spain.
Email: iperer02@estudiantes.unileon.es

Funding information
FEDER/Spanish Ministry of Science and Innovation-Agencia Estatal de Investigación) research project ISGEOMIN - ESP2017-89045-R; HYPOPROCKS (PDC2021-121352-100) by MCIN/AEI/10.13039/501100011033 and the European Union "NextGenerationEU"/PRTR

Abstract

Torrential rainfall regimes, among others, are the origin of accelerated soil erosion. The Spanish southeastern Mediterranean region is characterised by an arid climate regime affected by extreme erosion episodes with an important loss of sediments. Soil erosion effects are even more noticeable in areas where soil has been anthropically degraded, as in the mining district of *Sierra Minera de Cartagena*. The present research focuses on monitoring and mapping the changes in the sediment distribution of iron oxides and hydroxyl (OH^-) bearing minerals caused by a cold drop known in Spanish as 'DANA' in September 2019 on the *Rambla del Beal*. This short *rambla* is fed by sediments from its drainage basin and by mining residues, irrigating a wide agricultural area. When discharges overflow the *rambla* channel, residues spread over its floodplain and reach the ecological protected coastal lagoon *Mar Menor*. The objective of the study was mapping the mineral distribution of the mining materials eroded from the source areas and sedimented in *Rambla del Beal* during a DANA. The study was carried out using a pre- and a post-DANA image from the Sentinel-2 satellite. After masking vegetation, urban areas and water bodies, different band ratios (B4/B3, B11/B12, B8A/B6) and a Spectral Angle Mapper (SAM) classification were applied. Sediment deposits were identified in wider areas after the DANA. Iron oxides increased their extension by 11.08% in the central area (B3/B4 with R^2 of 0.84) and hydroxyl-bearing minerals increased by 8.95% in the *Rambla del Beal*'s headwaters (B11/B12 with R^2 of 0.71). The SAM classification (with a 0.1 rad threshold and an overall accuracy of 87.33%) allowed the differentiation and classification of two ferric iron oxides (haematite and goethite) and one iron hydrous sulphate mineral (jarosite). Additionally, band ratio images were spatially overlaid with the soil land uses map layer of the cadastre in order to plot the land uses most affected by the transported sediments during the DANA. These results highlighted agricultural land as the areas (land uses) most affected by iron oxides deposition, as oxidation processes occur more rapidly in these

areas. However, grassland and scrubland were the areas with the highest content of hydroxyl-bearing minerals, as water is accumulated in these places, which favours hydrolysis reactions.

Highlights:

- Torrential events can relocate large volumes of contaminated sediments from former mining areas.
- Sentinel-2 allows monitoring mine waste iron-sulphate changes caused by weathering alteration.
- Spatial mineralogical pattern in sediments is controlled by geomorphology and flood dynamics.
- The proposed digital image analysis allows mapping short-term evolution of mine waste sediments.

KEYWORDS

geomorphology, iron oxides, mine degraded soil, mineral distribution, multispectral, *Rambla del Beal*, remote sensing, water erosion

1 | INTRODUCTION

Soil degradation is one of the major global challenges that humans are currently facing and one of the biggest concerns in relation to agriculture and food security. Recently, soil erosion by water has been identified as the major soil threat in the European Union (EU), with a total soil loss rate of 9.7×10^8 t ha^{-1} year^{-1} (Panagos et al., 2015). Mediterranean countries are the most susceptible to this erosional process, representing the 67% of the EU's total annual soil erosion. In particular, Spain represents the 19.61% of the total annual soil loss in the EU (Panagos et al., 2015).

The main factors affecting soil loss by water are rainfall, topography, land or vegetation cover, and land use management (Panagos et al., 2020; Xia et al., 2020). These factors condition the degree of erosion. In the Spanish Mediterranean area, torrential rainfall behaviour is the main triggering element to active erosion events. This precipitation regimen with heavy rainfalls frequently has its genesis in Eastern Advection events associated with a cold drop referred to in Spanish as DANA (*Depresión Aislada en Niveles Altos*), which stands for Isolated High Level Atmospheric Depression (Martín-Vide et al., 2021). In the southeast of the Iberian Peninsula, one of the largest torrential rainfall episodes in terms of extent, intensity, and persistence in the last 50 years was the September 2019 DANA that affected the Region of Murcia. This episode took place between the 11–15 September 2019. However, precipitation was concentrated mainly on the 12th and 13th, and exceeded 200 mm in the *Sierra Minera de Cartagena* (AEMET, 2019), where the study area is located (Figure 1).

The *Sierra Minera de Cartagena* is one of the oldest mining districts in Europe, originating from the 5th century B.C. Mining activity has historically focused on lead (Pb), zinc (Zn), and iron (Fe), and the extraction was mainly from poly-metallic sulphide minerals deposits, such as galena (PbS), sphalerite (ZnS), and pyrite (FeS_2) (López-García et al., 1988). Currently, although activities have ceased, the environmental impact of mining is still evident, as tons of sulphide-rich waste dumps were accumulated over the *Sierra* (Figure 1h) (Robles-Arenas et al., 2006). These accumulations resulting from mining (present in tailings ponds and dumps) have a much higher water erosion rate than natural soils (García, 2004; Yadav et al., 2022), making erosion effects even more severe due to metal leaching and mobility from open mining locations. This, together with the ongoing weathering processes, has generated supergene products, including Fe and Al oxy-hydroxysulphates, carbonates, and hydrated sulphates (Fernández-Naranjo et al., 2020; Martín-Crespo et al., 2020). Al sulphate minerals, such as alunite ($KAl_3(SO_4)_2(OH)_6$) or jurbanite ($AlSO_4(OH)\cdot 5H_2O$), are products of the aluminosilicate mineral destructions. Fe secondary iron oxides and hydroxides, such as haematite (Fe_2O_3), schwertmannite ($(Fe^{3+})_{16}O_{16}(OH)_{9.6}(SO_4)_{3.2} \cdot 10H_2O$), or jarosite ($KFe_3(SO_4)_2(OH)_6$), come from the degradation of pyrite (FeS_2) due to oxidation processes as shown in Figure 2. Therefore, during floods generated by torrential rainfall

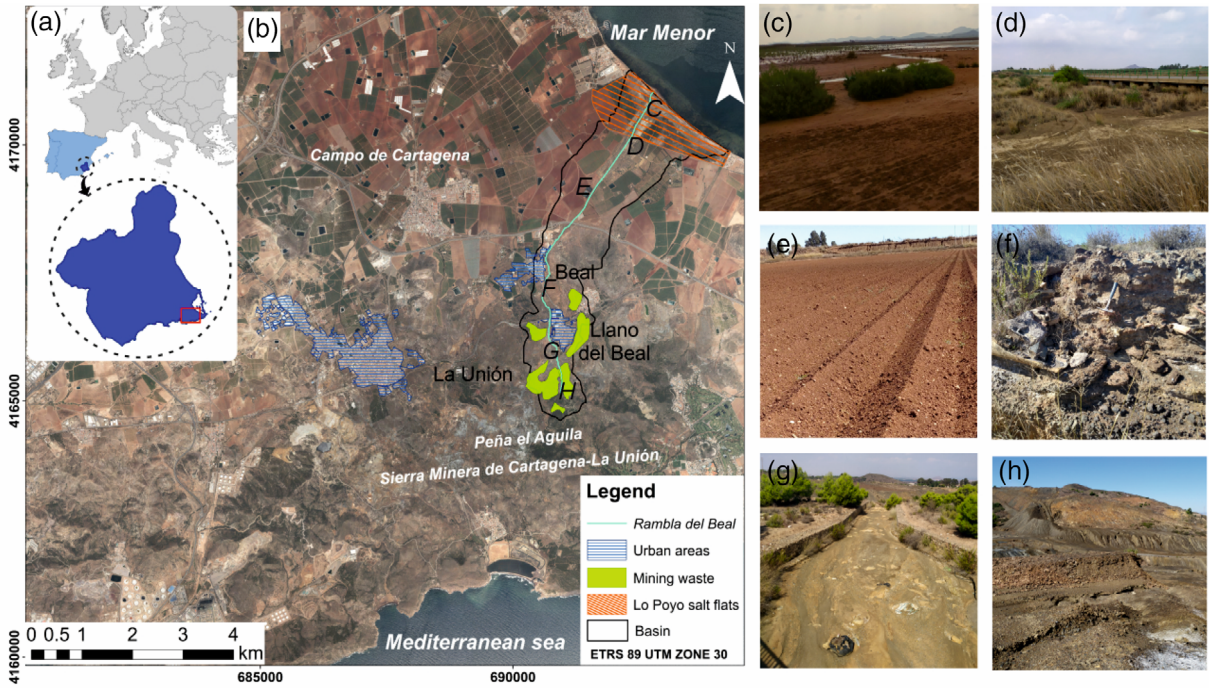

FIGURE 1 Study area located (a) in the southeast of Spain, within (b) the region of Cartagena and several photographs of the *Rambla de Beal*: (c) Lo Poyo saltmarsh on the river mouth sector of the rambla, (d) transition sector between the agriculture area and the final sector, (e) crop field on red calcareous soils in the centre of the basin, (f) mineral accumulation in sediments, (g) rambla channel with sediments in the headwater sector, and (h) mining waste dumps in the headwater sector

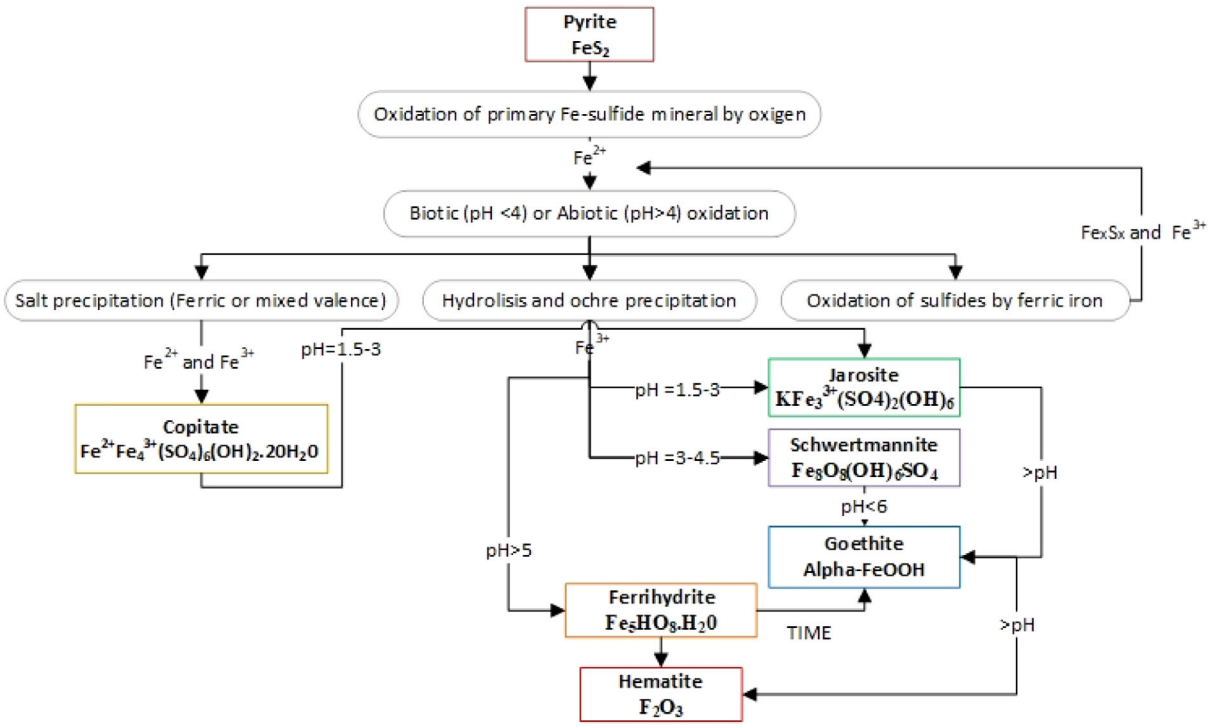

FIGURE 2 Model showing the formation of secondary iron oxides from pyrite oxidation in mine waste environments (Modified from: Zabic et al., 2014)

events, ephemeral channels (known as *ramblas*) transport a great amount of sediment (Figure 1f,g). These sediments include potentially hazardous materials present in the mining tailings, generating a contaminant

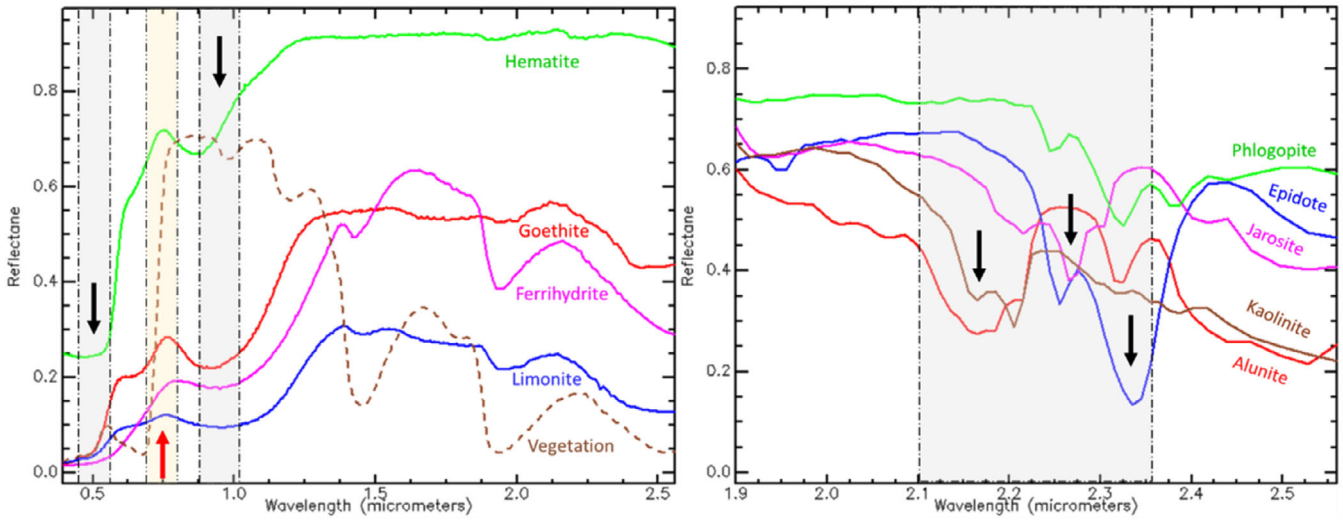

FIGURE 3 Spectral signature of iron oxides and vegetation (a; lefthand figure) and hydroxyl-bearing minerals (b; righthand figure). Between dashed lines are highlighted the wavelength ranges for the mineral characterisation. Black arrows show some of the absorption features and red arrows show the reflectance peaks (Data source: United States Geological Survey (2017))

sediment flow. These *ramblas* deposit their sedimentary load in floodplains in agricultural flat areas of *Campo de Cartagena* (Figure 1e), or in the form of low slope fluvial alluvial fans towards the *Mar Menor* (Figure 1c,d), a protected coastal lagoon of high ecological value. The *Mar Menor* lagoon is one of the most singular Mediterranean ecosystems. However, the lagoon is currently experiencing huge environmental impacts due to anthropogenic activities, major urban development, and the intensification of agriculture activities with fertilisers in recent years. All the previous impacts together with the former mining activity contamination have increased the ecosystem vulnerability (Velasco et al., 2017).

In order to analyse mineral mobility and distribution of contaminants because of the contaminant sediment flow in this context, remote sensing techniques were applied to Sentinel-2 Multispectral Instrument (MSI) sensor images. Nowadays, this technique offers a reliable alternative for mapping and assessing the mobility processes of metals and metalloids, as it allows systematic observation of large areas (Adiri et al., 2020; Azizi et al., 2022; de Sousa Mendes et al., 2022; Ge et al., 2020). It has been also largely applied in mining exploration to identify mining potential areas (Adiri et al., 2020; Cardoso-Fernandes et al., 2018; Lanfranchi et al., 2021), as well as to monitor environmental impacts derived from mining activity (Archarya & Kharel, 2020; Buzzi et al., 2016; Riaza et al., 2011). Mine wastes coming from open-pit operations (tailings or slurry ponds) are composed, among others, of gangue and non-useful ores. Most of these metals and hydrothermally altered minerals are spectrally active and have characteristic electronic and vibrational absorption features in the Visible and Near Infrared (VNIR) and Short Wave Infrared (SWIR) regions, which are reflected in their spectra, allowing them to be mapped (Xu et al., 2022; Zhang et al., 2022). However, to identify these spectral differences in the VNIR and SWIR region, a cloud-free image of dry bare soil is required. This makes remote sensing techniques especially suited to map mineral composition in semiarid regions. The low cloud and vegetation cover of these regions allow directly observation of topsoil mineral characteristics, which enables a better study of minerals' spectral properties.

Electronic processes are associated with metal ions (especially ferrous and ferric ions). Iron oxides present two absorption features and a reflectance peak in the VNIR (Figure 3a). The first absorption feature, located between 450 and 550 nm, is caused by the transitions of ferrous and ferric ions in different crystalline fields (Vijdea et al., 2004). This absorption feature overlaps with the chlorophyll absorption feature of vegetation, making it difficult to identify them individually (Richter, 2010). The second absorption feature, found between 800 and 1100 nm, is a consequence of the crystalline field of Fe^{2+} (Vijdea et al., 2004). Last, a reflectance peak is found between 600 and 700 nm and it is responsible for the typical red colour of iron oxides and hydroxides (haematite (Fe_2O_3), goethite (α-$Fe^{3+}O(OH)$), limonite ($FeO(OH)\cdot nH_2O$)) (Sahwan et al., 2020).

Vibrational absorption characteristics occur in the SWIR regions between the wavelengths of 2080 and 2350 mm (Xu et al., 2022) (Figure 3b). These processes involve the bonds in a crystal lattice or molecular compound. As it is the bond between the hydroxyl anion (OH^-), present in many hydrothermally altered materials, and different metals or metaloids, for example: Al-OH (i.e., alunite ($KAl_3(SO_4)_2(OH)_6$)

or kaolinite ($Al_2\ Si_2O_5(OH)_4$)), Mg-OH (i.e., phlogopite (K(Mg, Fe, Mn)$_3$Si$_3$AlO$_{10}$(F, OH)$_2$)) or Fe-OH (i.e., epidote ($Ca_2Fe^{3+}Al_2(Si_2O_7)(SiO_4)O(OH)$) or jarosite ($KFe_3(SO_4)_2(OH)_6$)), which are formed in different stages of hydrothermal alteration in the study area. They are included in the phyllosilicates 1:1 (kaolinite, phlogopite), sorosilicates (epidote), or sulphates (alunite, jarosite) groups. Phyllosilicates and sorosilicates are usually found around ore deposits and sulphates are associated with alteration product. These examples are only a few of the hydroxyl-bearing minerals that possess these vibrational spectral features, but there is a rich variety (Vijdea et al., 2004; Xu et al., 2022).

All these spectral characteristics allow remote sensing techniques to analyse the mineral distribution from the tailings dump to the sedimentation areas where they are deposited by fluvial dynamics (Adiri et al., 2020; Buzzi et al., 2016; Riaza et al., 2011). Therefore, the aim of this research is to map those mineral compositions eroded from the source areas and sedimented through the *Rambla del Beal* (in the southeast of Iberian Peninsula) during the DANA of September 2019, and those minerals formed during the following dry period, using a pre-DANA and a post-DANA Sentinel-2 images. Specifically, the objectives were to (1) characterise and obtain a relative quantification of the iron oxides and hydroxyl-bearing minerals present in the study area, (2) evaluate different remote sensing techniques for the study problem, and (3) map the minerals spatial distribution present in the mining waste dumps and in the sedimentation areas associated with the *Rambla del Beal*.

2 | STUDY AREA

The study area is the *Sierra Minera de Cartagena–La Unión* mining district, located in the Region of *Campo de Cartagena*, an agricultural region in the southeast of Spain. The study will focus on *Rambla del Beal* and its hydrological basin, one of the ephemeral drainage channels that flows into the *Mar* Menor (Figure 1).

A *rambla* is a watercourse typical of arid or semiarid areas which is normally dry except in medium or large floods. The *Rambla del Beal* has its source in the *Peña del Águila* relief. Its length is about 8 km and its catchment area is 8.7 km^2. The headwater sector runs through small peaks and valleys, passing near the villages of *Llano del Beal* and *El Beal*, where large mining deposits are located. Once past *El Beal*, the *rambla* reaches its lower sector, where it widens and flows through *Lo Poyo* saltmarsh, considered both a Site of Community Interest (SIC) and a Special Protection Area for Birds (SPAB).

The *Rambla del Beal*'s basin is considered one of the most polluted in the *Mar Menor* surrounding area. Approximately, 10.5% of the basin surface is occupied by dumps with high contents of heavy metals that are eroded and transported by water during torrential events (García, 2004).

The *Sierra Minera de Cartagena* belongs to the Internal Zones of the Betic Cordillera, also known as the "Alboran Domain", which is characterised by the structural stacking of three tectonic complexes (Nevado-Filábride, Alpujárride, and Maláguide). Each of them is impacted by a decreasing degree of metamorphism from bottom to top, both within each complex and over the entire series. Along the Almería-Cartagena volcanic belt (ACVB), significant calc-alkaline and shoshonitic volcanism (andesites, dacites, and rhyolites) occurred, whereas sedimentation took place within confined marine sedimentary basins. Volcanic activity spurred hydrothermal activity, resulting in the creation of significant Pb (Ag), Zn, and Sn ore deposits (Sanz de Galdeano, 1990; Torres-Roldán, 1979). Mineralization is mainly constituting two massive stratabound, locally named, *mantos*, which were economically interesting and, therefore, exploited.

The climate in the study area is semi-arid Mediterranean and characterised by highly irregular rainfall patterns, with extreme autumn rainfall events after a severe summer drought. This climate within xeric regimen conditions influences the development of both natural vegetation and soil. Natural vegetation is sparse and shrubby and soils lack the development of upper horizons. There are five main soils types, but only four of them have natural origin (Table 1). The other is a Technosol (FAO-WRB, 2007), an anthropogenic soil. The Technosols are young soils with mining origins and are rich in iron oxides and sulphates, lead, and zinc among other metals (Pellegrini et al., 2016). They are located in consolidated ponds and stabilised dumps. The Technosols present smectites in the clay fraction, which are dispersed when the presence of salts is high, thus forming fractures, where the washing process of fine material by water erosion is facilitated (Pellegrini et al., 2016). Therefore, these soils are the most vulnerable to erosion in torrential processes, as its deposits lack internal structure and consolidation. The second soil type is Gypsic Regosol (FAO-WRB, 2007), which presents a poorly consolidated fine-texture material and has a scarce evolution as it is highly altered with a gypsum accumulation in subsurface horizons. The next type is Haplic Cambisols (FAO-WRB, 2007), which present materials of aeolian, alluvial, or colluvial alteration. They have a limited use for agriculture, as they are very rocky, have a low base content and low thickness. The last soil type is Haplic Calcisols (FAO-WRB, 2007), which are formed by Quaternary materials of a calcic nature and whose main use is agriculture. If they present high calcium carbonate content

TABLE 1 Organic carbon content, calcium carbonate content, clay fraction, pH, and electrical conductivity (EC) from representative soils from the study area

Soil type	Organic carbon (%)	Calcium carbonate (%)	Clay fraction (%)	pH	EC mS/cm
Gypsic Regosol	1.0–1.1	40–60	20–40	8.4	0.2
Haplic Cambisol	0.1–1.0	30–40	20–30	8.0	0.6
Haplic Calcisol	2.0–3.0	50–70	20–30	8.2	0.5
Petrocalcic Calcisol	1.5–3.0	60–80	20–30	8.1	0.6

Source: Blanco-Bernardeau (2015).

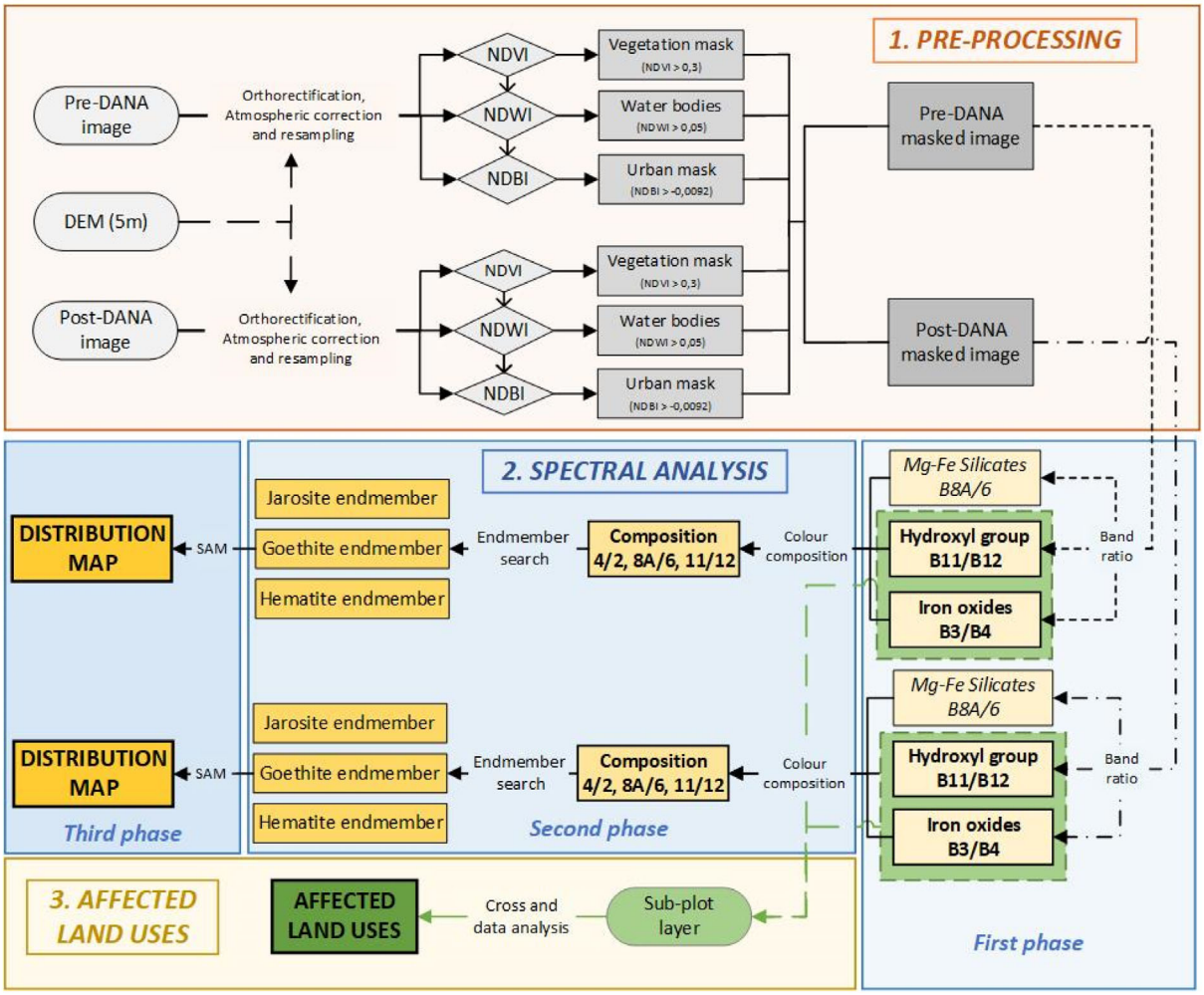

FIGURE 4 Methodological flow chart

(Table 1) or hardened layers of this material (petrocalcic horizons Ckm) within the first 100 cm of the surface (which is a limiting factor for the profile depth development), they are classified as Petrocalcic Calcisols. Gypsic Regosols, Technosols, and Haplic Cambisols (FAO-WRB, 2007) are found in the headwater sector and the *rambla*'s mouth, while Haplic and Petrocalcic Calcisols (FAO-WRB, 2007) are the predominant soil type in the central area, where agriculture lands are located. These agriculture areas are cultivated with artichoke, melon, broccoli, pepper, potato, wheat, cauliflower, and celery.

3 | MATERIALS AND METHODS

This section is organised into three different parts: image pre-processing, spectral analysis, and evaluation of land use affection (Figure 4).

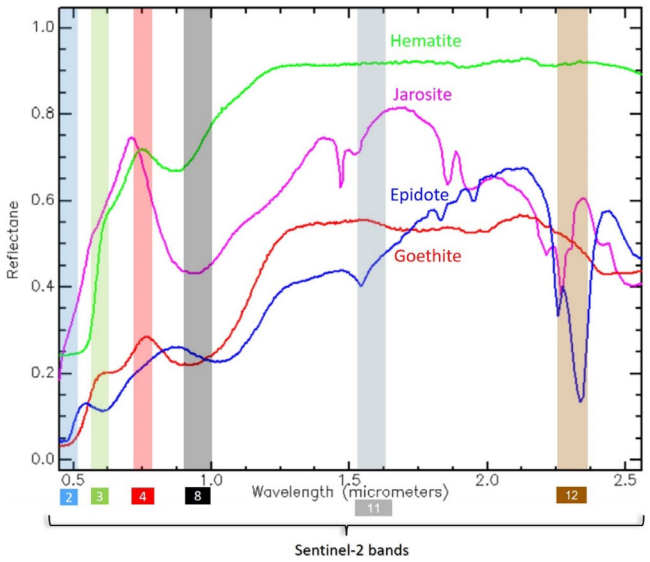

FIGURE 5 Iron oxides spectral curves and Sentinel-2 bands' wavelength ranges for their characterisation (Data source: United States Geological Survey (2017))

3.1 | Image pre-processing

This study was carried out using images from the twin satellites Sentinel-2A and Sentinel-2B. Their MSI sensor is one of the most suitable to study iron oxides and altered minerals, as several of the sensor bands are located over the main absorption and reflection features (Mielke et al., 2014). On the one hand, the satellite's band 8A (λ_{NIR2}) centred at 865 nm is particularly suited for the detection of iron oxides (European Space Agency, 2015). On the other hand, Sentinel-2 band 12 (λ_{SWIR2}), captures the vibrational absorption processes occurring between 2100 and 2280 nm (Figure 5), for the identification of the OH^- anion. Thus, Sentinel-2 becomes one of the most effective multispectral satellites for the identification of hydrothermally altered minerals (Ge et al., 2020).

3.1.1 | Image corrections and resampling

In order to study the effects derived from the September 2019 DANA, a pre- and post-event analysis has been carried out using images from 19 August 2019 to 10 October 2019, respectively. Both images were downloaded with a 1C processing level from the Copernicus Open Access Hub web server. Therefore, they had been already radiometrically processed with reflectance values of the top of atmosphere (TOA) and orthorectified with a DEM of 90 × 90 m spatial resolution (European Space Agency, 2019). However, in areas with steep relief such as the *Sierra Minera de Cartagena*, there are still geometrical distortions in pixel values. To improve the result, images were orthorectified using the *sen2Cor* (European Space Agency, 2018) processor integrated in the R library *sen2r* (Ranghetti et al., 2020). For this purpose, a 5 × 5 m spatial resolution DEM was used, derived from LiDAR data and freely available on the Spanish CNIG (National Geography Information Centre) website. Simultaneously with the *sen2Cor*, atmospheric corrections (cirrus corrections, aerosol optical thickness retrieval and water vapour retrieval) were applied using the default parameters for mid latitudes (Richter et al., 2012). The objective of this last operation is to obtain reflectance values.

The selected bands showed different spatial resolution, so the next step was resampling both images into 10 m, as it is considered the most optimal spatial resolution to study minerals with the available dataset (Ge et al., 2020). This process was carried out using the "Super-Resolving Multi-resolution Images" method with the *Sen2Res* processor incorporated in the Sentinel Application Platform (SNAP) version 8.0. Even though this method is very similar to the "Panchromatic refinement", it does not use a panchromatic band (non-existing in Sentinel-2) and instead uses the 4 bands at 10 m resolution to build a model of how the information is shared in these bands, and what information is specific to each band (Brodu, 2017).

3.1.2 | Vegetation, water body, and urban masks

In mineralogy spectral studies, it is common to mask some elements such as vegetation or water bodies to avoid interference and excessive noise in the images (Cardoso-Fernandes et al., 2018). Commonly, to mask each element, it is necessary to generate band ratios that highlight the studied element, so it can be characterised and excluded from the study area.

Vegetation is one of the most important elements to mask in spectral studies applied to geology, since the absorption feature of chlorophyll in the green wavelength range interferes with the first absorption feature of iron (Kariuki & Van der Meer, 2003; Koch, 2000). For this purpose, the Normalised Difference Vegetation Index, (NDVI) was generated (Equation 1). As a threshold value between the pixels considered with and without vegetation, it was set at 0.3. According to Chen et al. (2021), this threshold masks the lusher vegetation, so even if there are areas with dry vegetation left unexcluded, there will be no interference with the mineral analysis.

$$\mathrm{NDVI} = \frac{\mathrm{B8} - \mathrm{B4}}{\mathrm{B8} + \mathrm{B4}} \quad (1)$$

Roofs in urban areas can also interfere with the absorption and reflection features of iron due to the reflectance peak from the building material in the red wavelength. In this case, the band ratio used is the Normalised Difference Built-up Index (NDBI) (Equation 2) proposed by Zha et al. (2003). The threshold value of the urban areas was established by visual observation at −0.0092, which is similar to the threshold obtain by other authors (Hua et al., 2012; Karimi et al., 2019).

$$\mathrm{NDBI} = \frac{\mathrm{B12} - \mathrm{B11}}{\mathrm{B12} + \mathrm{B11}} \quad (2)$$

The last applied mask was to eliminate the noise of the water bodies, due to the presence of both the Mediterranean Sea and the *Mar Menor* lagoon. The band ratio used is the Normalised Difference Water Index (NDWI) (Equation 3) proposed by McFeeters (1996). It was established at threshold value of 0.05 for the pre-DANA image, and at 0.23 for the post-DANA image, by visual analysis. In this case, the different threshold values derive from the different algae, phytoplankton, or chemicals' concentration available in the *Mar Menor* in each period: the transportation of fertilisers during the DANA caused an increase of the reflectance value (Banguira et al., 2019; Du et al., 2016)

$$\mathrm{NDWI} = \frac{\mathrm{B3} - \mathrm{B8}}{\mathrm{B3} + \mathrm{B8}} \quad (3)$$

The three ratios were applied individually to the pre- and post-DANA images obtaining a total of six masks. These six masks were summed up and applied on both images in order to mask the same number of pixels in the pre- and post-event image so that later a comparison could be made within the same surface.

3.2 | Spectral analysis

Once the pre-processing was completed, the next step was the spectral analysis based on band ratios and a Spectral Angle Mapper (SAM) classification. Band ratios allowed a quantitative differentiation of areas with a higher or lower contents of the elements under study (iron oxides and hydroxyl-bearing minerals). Also, band ratios were combined into a colour composition allowing the observation of the distribution of all the study minerals in just a single image. The SAM classification allowed differentiation between three iron oxides and hydroxides with very similar curves.

3.2.1 | Band ratios

Mineral composition is one of the main factors controlling absorption features in spectral signatures. Variations in the spectral curve are related to chemical composition (absorptions due to electronic transitions) and crystalline structure (absorptions due to vibrational processes) (Van der Meer, 2001). To analyse these differences, absorption-band parameters such as wavelength position and depth have been used to quantitatively estimate soil composition (Van der Meer, 2004).

Furthermore, mineral absorption features can be analysed by band ratios that are designed to enhance the spectral contrast in the wavelength of the absorption feature. As a result, band ratios are used to express the depth of the absorption feature and to relatively quantify the target material. Band ratios have been proven successful in imaging spectroscopy for the estimation of different soil components, for example, iron oxides (Rowan & Mars, 2003; Sahwan et al., 2020) or hydroxyl-bearing minerals (Van der Meer et al., 2012).

For the study area, it two band ratios were proposed to study different minerals groups: (i) iron oxides, and (ii) hydroxyl-bearing minerals. These band ratios were used to study each mineral group individually. Additionally, a Fe-Mg silicates band ratio was generated. Thereafter, the three band ratios were combined to generate a colour composition that showed the area affected by all the study minerals. Also, the colour composition was used to obtain endmembers for the SAM classification.

Iron oxides band ratio

For the identification of iron oxides, the reflectivity peak in the red wavelength (600–700 nm) must be considered, as well as the decrease in the green region (500–570 nm) (Sahwan et al., 2020). Following these characteristics, Rowan and Mars (2003) and Rowan et al. (2005) proposed the following band ratio (Equation 4) adapted now for Sentinel-2 images.

$$\text{Iron oxides} = \frac{\mathrm{B4}}{\mathrm{B3}} \quad (4)$$

Hydroxyl-bearing minerals band ratio

For the identification of hydroxyl-bearing minerals, the reflectance peak in band 11 (λ_{SWIR1}) and the absorptions area caused by the vibrational processes in the wavelengths of band 12 (λ_{SWIR2}) were considered. Following these characteristics, authors such as Sabins (1999) or Van der Meer et al. (2012) proposed the following index (Equation 5) adapted now for Sentinel-2 images.

$$\text{Hidroxyl group} = \frac{\mathrm{B11}}{\mathrm{B12}} \quad (5)$$

Band ratios performance was validated with laboratory spectral data of 12 soils samples collected over the Beal rambla. The spectral curve of the 12 soil samples was obtained and then compared with the pre-DANA band ratios, as the weather conditions on both the dates of sample collections and pre-DANA image acquisition were very similar. Linear regression analyses were performed both for iron oxides and hydroxyl-bearing minerals band ratios between Sentinel-2 pre-DANA image and soil samples laboratory spectrum.

Additionally, a band ratio was generated for the identification of Fe and Mg silicates, such as olivine or pyroxene. This band ratio was generated in order to highlight possible minerals which contain iron, but not in its oxidised form, in the colour composition. The reflectance peak located in band 8A (λ_{NIR2}) and the absorption feature occurring at wavelengths in band 6 (λ_{RED2}) were considered. Following these features, Githenya et al. (2019) proposed this band ratio: B8A/B6.

3.2.2 | SAM classification

This analysis is a supervised classification that compares the angle between the vector of a reference spectrum or endmember $\left(\vec{r}\right)$ and the vector of a spectra obtained from a given pixel in the image $\left(\vec{t}\right)$, applying the following equation (Equation 6) (Kruse et al., 1993):

$$\alpha = cos^{-1}\left(\frac{\vec{t}\cdot\vec{r}}{\left\|\vec{t}\right\|\cdot\left\|\vec{r}\right\|}\right) \quad (6)$$

In this way, there will be the same number of resulting images as the number of endmembers. These images will show binary values: those pixels whose spectral curves are more similar to the endmember present at lower angle and are classified as belonging to the analysed class, while those pixels that exceed the angle threshold are excluded. In this research, the angle threshold was set to 0.1 rad, following the recommendation of Masoumi et al. (2017). This low value ensures that those classified pixels truly corresponded to the endmember class.

In the present study, the endmembers' pixels have been taken directly from the image itself: two pixels of iron oxides—haematite and goethite—and one iron hydroxide—jarosite—(Figure 6). The endmembers were selected using both the colour composition and the spectral signatures from the USGS Spectral Library (United States Geological Survey (2017)). First, in the colour composition in those areas where the iron oxides are sedimented (goethite and haematite) and where the iron hydroxide was precipitated (jarosite) were located. Then the spectral signatures of the image pixels located in these areas were compared with the ones from the USGS Spectral Library. For this comparation, the USGS spectral signatures were spectrally resampled to the Sentinel-2 spectral resolution. As a result, it can be seen that the three selected reference curves show different spectral features. Haematite is characterised by a maximum reflectance peak near 0.78 μm (Band 6), and an absorption feature minimum near 0.84 μm (Band 8A). Goethite presents its maximum reflectance feature close to 0.74 μm (Band 6), and its absorption feature lowest point is located at 0.94 μm (Band 9). Jarosite reflection peak is characterised by a maximum at 0.70 μm (Band 5) and an absorption feature near 0.94 μm (Band 9). So, each mineral has a unique combination of bands where the reflectance and absorption feature are located. Moreover, at 0.6 μm, goethite shows a reflectance feature while haematite and jarosite do not show any changes. On the other hand, jarosite has a larger difference between the wavelengths of 1.6 (Band 11) and 2.5 μm (Band 12), due to the vibrational processes generated by the bonding of the iron and the hydroxyl (absorptions feature in the SWIR).

The resulting cartography from the SAM classification was validated with laboratory soil data extracted from Robles-Arenas (2007), Pérez et al. (2013), and Belmonte et al. (2017). For this purpose, a spatial overlay analysis was performed between the classified image and the coordinate data from the soil samples obtained in the previously mentioned research. Additionally, a confusion matrix was generated to assess the accuracy of the classification by comparing the SAM results with ground truth Regions of Interest (ROIs). Ground truth ROIs were delimited based on sediment and water dynamics of the rambla. ROIs were established in the same geomorphological units as the three endmembers used in the SAM classification (haematite, goethite, and jarosite). It is assumed that within the same geomorphological unit controlled by the same dynamics, the sedimented and precipitated minerals will be the same. The endmembers used for the SAM classification were excluded in the ground truth ROIs.

3.3 | Soil land uses affected by the mining waste transport

The impact of sediments from mining waste has a great variation depending on the existing land use and on the mineral quantity. The land use was extracted from two sources. The first and main one was the cultivation subplot layer from the Spanish cadastre (Ministry of finance

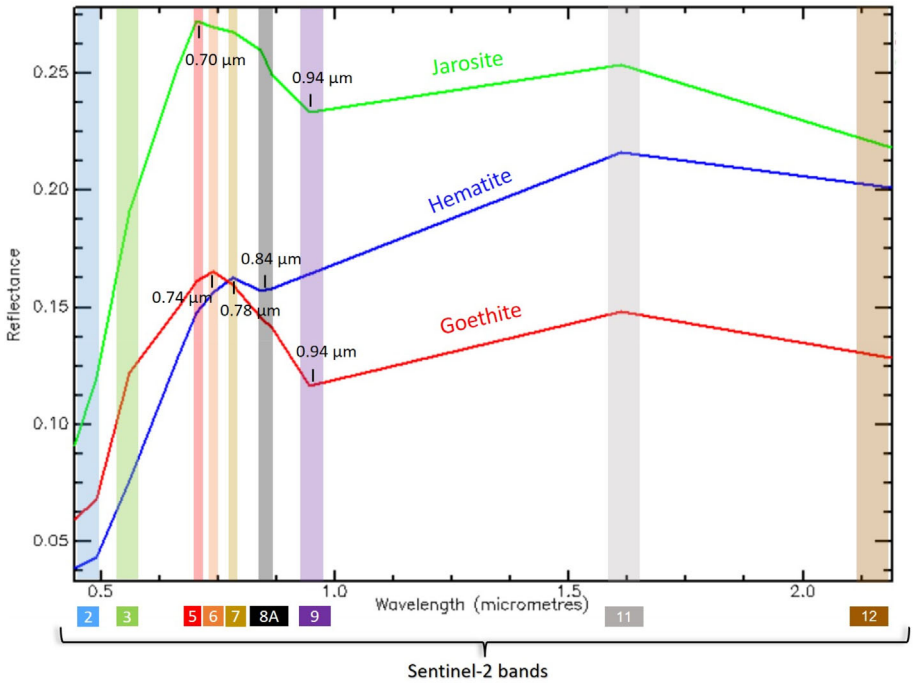

FIGURE 6 Spectral features of goethite, haematite, and jarosite obtained from the Sentinel-2 image on the *Rambla del Beal* and Sentinel-2 bands' wavelength ranges used for their characterisation. In this case, the main absorption and reflectance features of each iron mineral are presented

and civil service, 2022). The second one was another national land use layer, the SIOSE (Spanish Land Use Information System) cartography (MITMA, 2017). Those polygons without land use in the cadastre were classified as herbaceous crops according to the SIOSE, so they were assimilated with irrigated arable land class from the land parcel layer. In total, there were 14 land classes. However, four of them had less than 40 m^2 in the study area, so they were excluded (non-irrigated carob orchards, non-irrigated almond orchards, irrigated orchards and roads and highways). Also, the railway land use class in cadastre cartography was changed because they had assigned this class based on the ownership of the land (railway company). Again, these polygons were assimilated to scrubland class, since the majority of the area of this class was occupied by this type of vegetation in SIOSE cartography. Of the remaining nine land use classes, seven corresponded to vegetation covers (timber pine forest, grassland, and scrubland) and agriculture areas (irrigated and non-irrigated agriculture, irrigated citric orchards, and non-irrigated orchards), which were supposed to be masked by the previous vegetation mask. However, because of aridity climate conditions of the study area, especially in the summer and autumn months (when the study images where acquired), most of these pixels are bare land, and so they were included in the analysis area.

The final land use layer was spatially compared with each resulting layer from the following band ratio operations: two raster layers for the relative content of iron oxides and two raster layers for the content of hydroxyl-bearing minerals, one of each for the pre-DANA and the other one for the post-DANA situation. The resulting tables were analysed in order to determine to what degree the sediments from mining waste affected the surrounding land.

4 | RESULTS

The application of the proposed method has achieved different results that are outlined below.

4.1 | Distribution of iron oxides

Figure 7 shows the spatial distribution of iron oxides obtained from the specific band ratio (B4/B3). This band ratio displays elevated values, especially after the rainfall event that suggest the presence of iron oxides (Table 2). Previous research in a nearby area placed the value 1.3 as the threshold to indicate the presence of iron oxides with this band ratio (Pereira, 2020).

Figure 7 zone I points out the *rambla*'s mouth as the area with the greatest iron oxide sedimentation. At the same time, a little washout in the iron sediments due to the DANA can be seen, but still with high contents, in the crops located on the central area (Figure 7 zone II). On the other hand, the source area in the south of the image does not show high iron oxide contents, neither in the pre- nor in the post-DANA image (Figure 7 zone III). This sedimentation process is also reflected in the increase of both the average value and the area affected by the iron from the pre-DANA scenario to the post-DANA (Table 2).

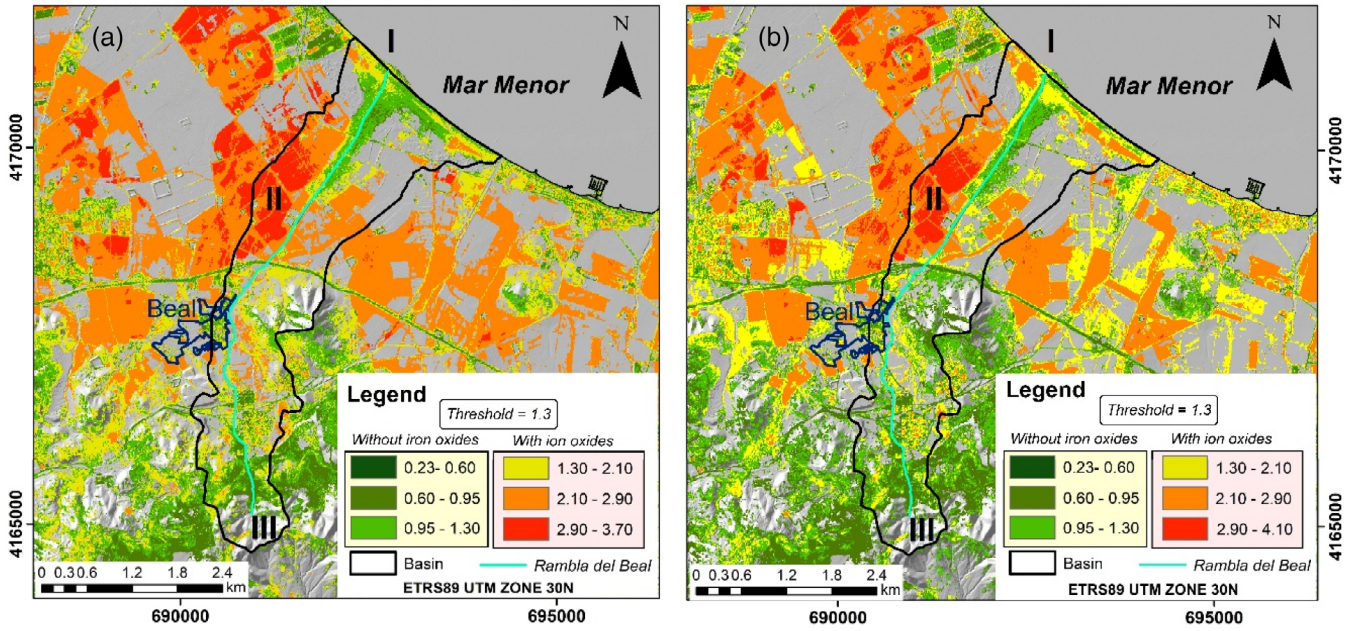

FIGURE 7 B4/B3 ratio for the identification of altered minerals with iron oxides presence in (a) pre- and (b) post-DANA situations. Both images show: (I) in the final sector of the rambla, (II) in an area of crop fields of the centre of the basin, and (III) in the headwaters sector of the basin

TABLE 2 Band ratio range, threshold, average, and affected surface analysed values of the iron oxides (orange) and hydroxyl-bearing minerals (green) band ratios

	Iron oxides		Hydroxyl-bearing minerals	
	Pre-DANA	**Post-DANA**	**Pre-DANA**	**Post-DANA**
Band ratio range	0.23–3.7	0.23–4.1	0.43–2.23	0.38–2.90
Threshold	1.30		1.10	
Average value	2.32	2.38	1.15	1.21
Affected surface	56.57%	67.65%	73.33%	82.28%

Figure 8a shows the comparison of iron oxides band ratio estimated from the Sentinel-2 image and from soil samples laboratory reflectance data (Figure 8b). This linear regression obtained a coefficient of determination $R^2 = 0.8356$. Based on this result, there is a good relationship between the Sentinel-2 image and laboratory spectral data.

4.2 | Distribution of hydroxyl-bearing minerals

The results from the band ratio for the identification of hydroxyl-bearing minerals (B11/B12) are shown in Figure 9. Again, the high values of the band ratio (Table 2) indicate the presence of altered minerals. Previous studies have established a threshold for this specific band ratio for hydroxyl-bearing minerals in 1.1 (Franto & Donny, 2018).

Once more, the results show an increase of the area affected by mineral sedimentation and precipitation after the DANA (Table 2). The first area is the *rambla*'s mouth, coinciding with *Lo Poyo* saltmarsh (Figure 9 zone I). The crop fields of the basin's central area are the second location (Figure 9 zone II). Finally, there is a high concentration of hydroxyl-bearing minerals in the headwaters sector, which has increased even more after the rainfall event (Figure 9 zone III). Also, the sedimentation and precipitation process are reflected in the increase of both the average value and the area affected by the hydroxyl-bearing minerals from the pre-DANA scenario to the post-DANA (Table 2).

Figure 10a shows the comparison of hydroxyl-bearing minerals band ratio estimated from the Sentinel-2 image and from soil samples laboratory reflectance data (Figure 10b). This linear regression obtained a coefficient of determination of $R^2 = 0.7061$. Based on this result, there is a good relationship between Sentinel 2 image and laboratory spectral data.

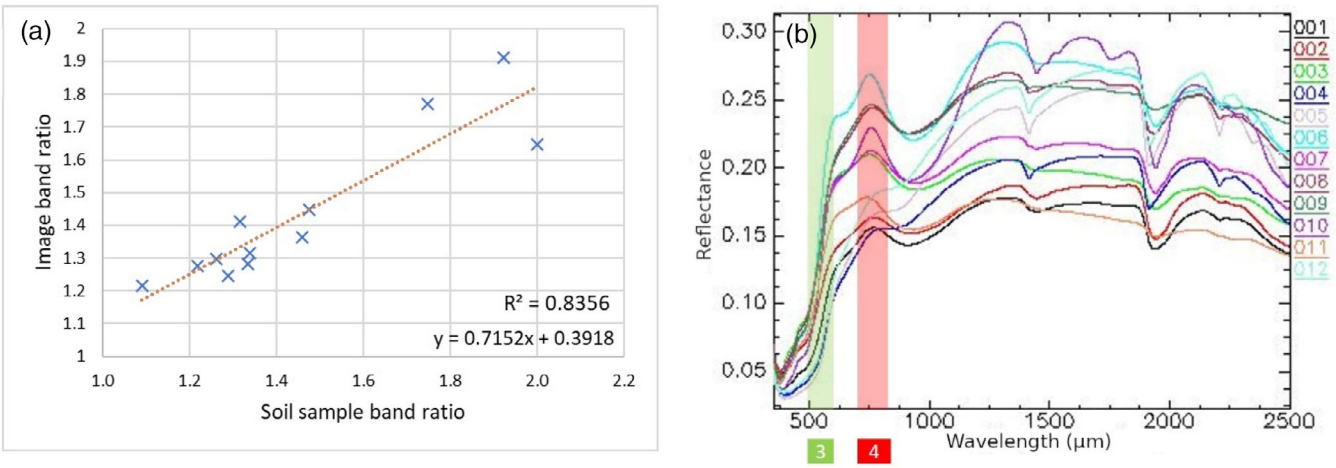

FIGURE 8 (a) Scatterplot and linear regression of iron oxides band ratio calculated from Sentinel-2 pre-DANA image and laboratory soil sample spectrum. (b) Soil samples laboratory spectral curve and Sentinel-2 band used in iron oxides band ratio

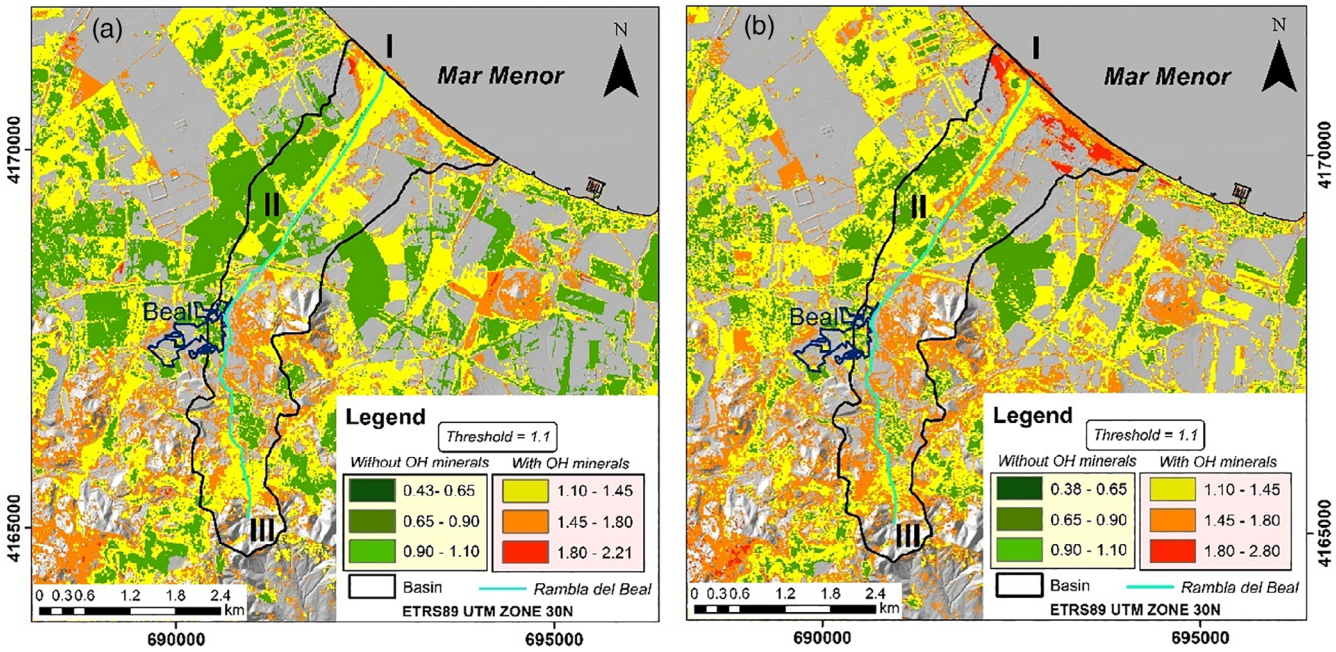

FIGURE 9 B11/B12 ratio for the identification of hydroxyl-bearing minerals in (a) pre- and (b) post-DANA situations. Both images show: (I) in the final sector of the rambla, (II) in an area of crop fields of the centre of the basin and (III) in the headwaters sector of the basin

4.3 | Distribution of haematite, goethite, and jarosite

Taking the spectral curves shown in Figure 6 as end-members, a SAM classification was performed to map three iron minerals: jarosite, goethite, and haematite. Figure 11 shows the distribution of these minerals in the study area. Haematite is mainly found in the crop fields of the central area, jarosite is located only at the *rambla*'s mouth, and goethite is present both at the *rambla*'s mouth and in the headwaters sector, areas where there is greater water accumulation (waste dumps and open cuts).

Both pre and post-DANA maps show a similar spatial distribution. The most remarkable difference is that in the pre-DANA image, there is less jarosite and a higher content of goethite, and that there is a decrease in the surface of the sediments corresponding to haematite on the crop fields of the post-DANA image (Table 3).

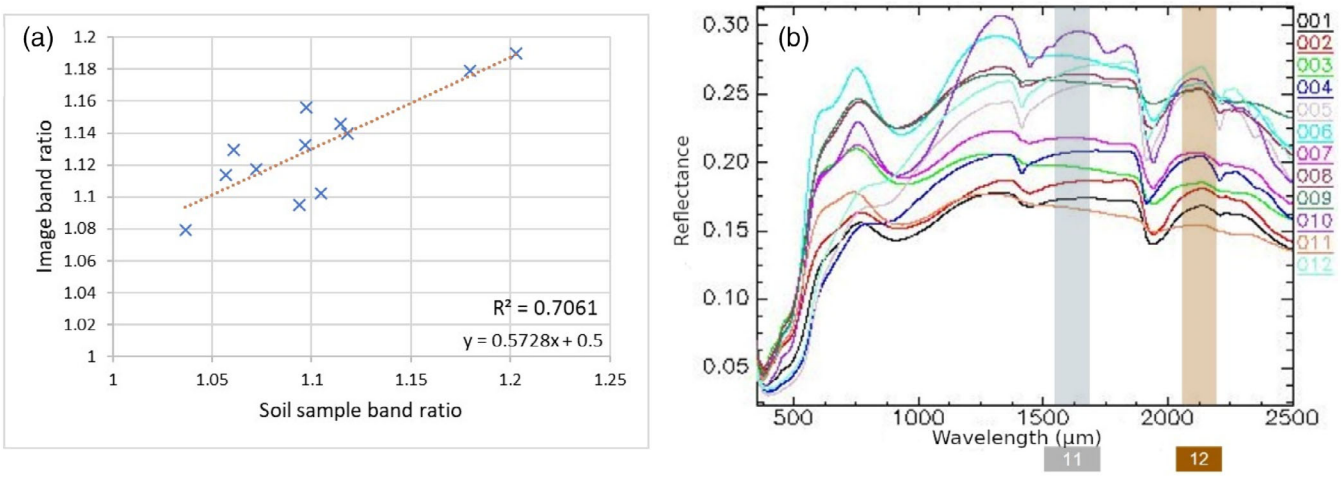

FIGURE 10 (a) Scatterplot and linear regression of hydroxyl-bearing minerals band ratio calculated from Sentinel-2 pre-DANA image and laboratory soil sample spectrum. (b) Soil samples laboratory spectral curve and Sentinel-2 band used for hydroxyl-bearing minerals band ratio

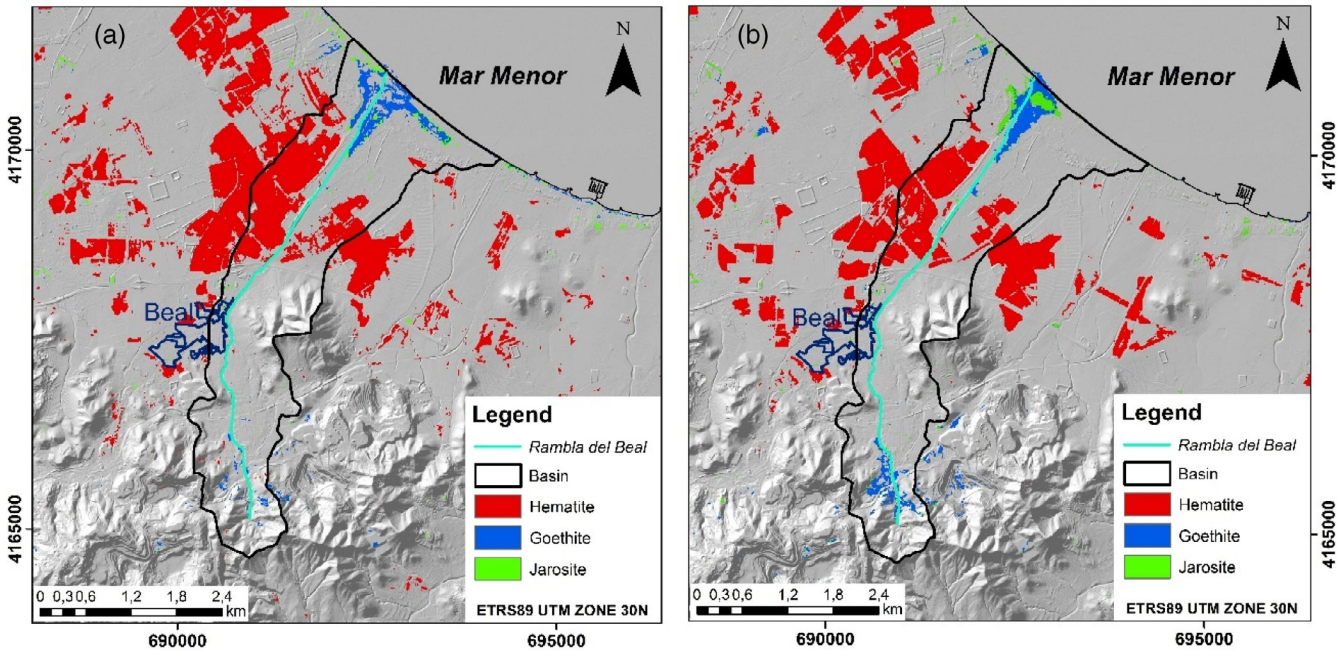

FIGURE 11 Distribution of haematite, goethite, and jarosite in the study area in a) pre-DANA and (b) post-DANA

Table 4 shows the accuracy of the SAM classification. Haematite shows the best accuracy with 95%, and jarosite the worst with 78%. The overall accuracy for the SAM classification is 87.33%.

Finally, Figure 12 shows the colour composition base on the band ratios: 4/3, 8A/6, and 11/12. In this composition, pink-reddish colours represent areas with a high presence of iron oxides, while green colours correspond to Mg-Fe silicates and purple-blue colours are associated to hydroxides. The *rambla*'s mouth is the area where both hydroxyl-bearing minerals and iron oxides concentration has clearly increase after the DANA (Figure 12 zone I). On the other hand, in the crop fields located in the central area of the basin (Figure 12 zone II), the orange-pinkish colour of the pre-DANA image (Figure 12a) has changed to a more yellowish-orange colour in the post-DANA image (Figure 12b), which seems to indicate a washout of iron oxides. The source area, located in the headwaters sector of the basin, in both images has bluish colours indicating the presence of hydroxyl-bearing minerals that are accumulated in the mining wastes (Figure 12 zone III).

Haematite		Goethite		Jarosite	
Pre-DANA	**Post-DANA**	**Pre-DANA**	**Post-DANA**	**Pre-DANA**	**Post-DANA**
132.21	107.50	44.82	39.35	2.51	13.49

TABLE 3 Affected surface area (ha) of the iron oxides (orange) and hydroxyl-bearing minerals (green) band ratios

		Classified				
		Haematite	**Goethite**	**Jarosite**	**Non-classified**	**Accuracy (%)**
Predicted	Haematite	**1425**	0	0	75	**95**
	Goethite	0	**1335**	120	45	**89**
	Jarosite	0	150	**1170**	180	**78**

TABLE 4 Confusion matrix for SAM classification (pixels)

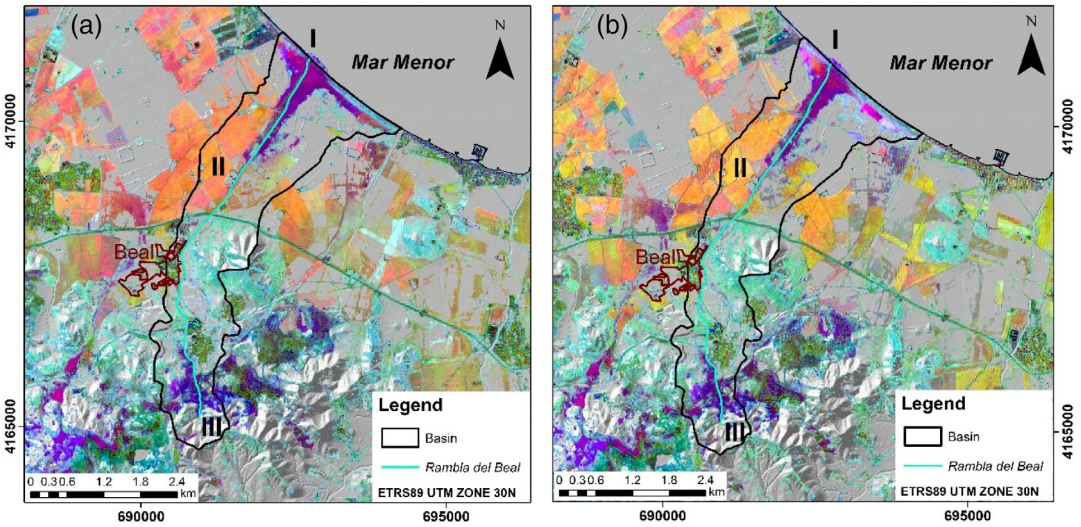

FIGURE 12 Colour composition (4/3, 8A/6, 11/12) a) pre and (b) post DANA. Both images show: (I) which corresponds to the rambla's mouth, (II) which crop fields are in the centre of the basin and (III) headwaters sector of the basin. The orange-pinkish colours show a greater presence of minerals with iron oxides and dark blue the presence of hydroxyl-bearing minerals

4.4 | Cross checking with soil land uses affected by the 2019 DANA

The results on Table 5 show that from pre-DANA scenario, the most affected area by iron oxides corresponds to irrigated agriculture, irrigated citric orchards, and dry drainage network (*rambla*'s mouth) land uses. In the scenario post-DANA, the most affected areas are located again on the irrigated agriculture and irrigated citric and non-irrigated agriculture, although non-irrigated agriculture appear as a new class. All of them are part of the floodplain and flooded terraces, which favour the conditions for the sedimentation of iron oxides. The classes that have most relatively increased their affected surface are: scrubland, timber pine forest, and non-irrigated agriculture. Only the dry drainage network class decreased its iron content due to the DANA.

On the other hand, the most affected areas in the pre-DANA scenario by hydroxyl-bearing minerals correspond to dry drainage network, scrubland, and non-irrigated orchards land uses. In the post-DANA scenario, again the most affected areas correspond to the dry natural hydrography network, and scrubland, incorporating grassland as a new class. The three classes are located on the *rambla*'s mouth (several tens of meters width), where water accumulation occurs over a longer period of time, which favours the formation processes of these minerals. The classes that have most relatively increased their affected surface because of hydroxyl-bearing minerals are: non-irrigated agriculture and irrigated agriculture. On the contrary, the only class that decreases its content of hydroxyl-bearing minerals is the unproductive.

5 | DISCUSSION

5.1 | Origin and effects of iron oxides and hydroxides: Evolution and distribution

The results show that the *Rambla del Beal* is an area strongly affected by sedimentation from mining waste products from mineral alteration and/or mineral neoformation under short variable and extreme conditions, which are highly correlated to oxidising and reducing environments influenced by flood activity. It was possible to characterise two different processes, that appeared spectrally different. On the one hand, hydroxyl-bearing minerals are found in grassland and scrubland areas, where water is accumulated, favouring hydrolysis reactions and, therefore, their precipitation in a following dry period (Byrne et al., 2012; Fan et al., 2022). These minerals are predominant in the sediments, as they occupied a bigger extension both in the pre- and post-DANA scenario (Table 2). Hydroxyl-bearing minerals are precipitated in irregular tailing ponds of variable size over the dump surfaces, that are currently being eroded, and in the distal saltmarsh areas around the *rambla*'s mouth. The fact that hydroxyl-bearing minerals are predominant in the irregular dump surfaces reflects the complex topography and the mining disturbance in these areas. This behaviour is in line with the spatial distribution of mine contaminants observed by Riaza et al. (2011), Archarya and Kharel (2020), and Pan et al. (2022) in other study areas.

On the other hand, iron oxides are mainly found on agricultural lands, corresponding to sedimentation areas such as floodplains where oxidisation processes occur more rapidly due to better drainage and superficial deposition with intense alteration. Additionally, soil alkaline pH (Table 1) favours precipitation of iron oxides (Anawar, 2013; Kicińska et al., 2021). Even though, iron oxides' spatial distribution is more restricted than hydroxyl-bearing minerals (Table 2), as they reach higher surface extensions. Authors such as Belmonte et al. (2017) have estimated that there is up to 67,700 ppm of bioavailable iron in the top soil occupied by the crops. This high metal concentration may be negatively affecting the crops' growth as Diedhiou et al. (2020) and Rasheed et al. (2020) have observed. Iron excess in plants can displace cell redox balance into a pro-oxidant state, which may produce cell death because of oxidative stress, reducing plant growth and crop productivity (Diedhiou et al., 2020). A high metal content in soil can lead to morphological, metabolic, physiological, and molecular aberration, such as chlorosis of leaves or enzymatic peroxidation of membranes (Singhal et al., 2022). However, no studies of iron uptake by crops has been carried out in the nearby intensive agricultural lands. Furthermore, if these results are compared with the soil map (Ramírez et al., 1999), the soil type present in the agricultural region (Haplic Calcisol) cannot give rise to such elevated levels of iron oxides, which may be indicating a potentially hazardous situation for crops (Elberling et al., 2010; Jordán-Vidal et al., 2020).

This mineralogical pattern between the sediment's locations and the flood dynamics is even more evident when observing the spatial and temporal distributions of the iron oxides (haematite and goethite) and iron hydroxide (jarosite) deposits (Figure 11). Their spatial and temporal relationships correspond to iron secondary mineralization processes (Figure 2), due to the fact that they are product of different pyrite weathering oxidation processes. In Figure 11, it can be seen how pyrite has been transformed into goethite and jarosite, as their surface extension increased after the DANA, similar to that shown in Fan et al. (2022) and Pan et al. (2022) in other areas. Especially, jarosite is not found in the pre-DANA scenario, as it is a metastable mineral that rapidly transforms into haematite or goethite, as shown in Fan et al. (2022) and Pan et al. (2022). Both goethite and jarosite are found in areas with greater waterlogging accumulation also appearing when redox conditions are alternated and, therefore, after oxidation and hydrolysis reactions mineral precipitation takes place (Byrne et al., 2012; Fan et al., 2022). Also, it is noticeable that the presence of jarosite is most likely indicating the generation of Acid Mining Drainages (AMD), as an extremely acid pH (<3) environment is needed for its precipitation (Fan et al., 2022; Shi et al., 2015). So, it is supposed that on the surface formation, the runoff water pH is lower due to the free ferric phases acting as sulphides oxidizers, and silicate acid hydrolysis allowing latter formation of jarosite (Creeper et al., 2012; Grealish & Fitzpatrick, 2013; Shi et al., 2015). These jarosite deposits are indicating that the mineral deposits mapped are recent, since they have not turned into other more evolved oxides after alteration due to more intense weathering oxidising conditions. On the other hand, haematite is distributed throughout the floodplain crop fields where there is good drainage and the effect of atmospheric exposure is evident, under prevailing oxidising conditions. Haematite is the most common of the three ferric phases, both in the pre- and post-DANA situation. This large presence is due to the weathering oxidation in the dry season, that causes jarosite and goethite to change phase and transform into more stable mineral phases such as haematite. This new scenario shows a more intense grade of alteration and evolution while the oxidation processes advance.

TABLE 5 Percentage of surface of each land use in the *Rambla del Beal* area with presence of iron oxides (orange) and hydroxyl-bearing minerals (green) in the pre- and post-DANA scenarios. In blue, land uses with a higher percentage of affected surface are marked. The dark orange and dark green columns show the percentage difference in the area covered by these minerals between the pre and post DANA scenarios. Those with higher values are shown in red

	Iron oxides			Hydroxyl-bearing minerals		
	Pre-DANA	Post-DANA	Difference pre and post (%)	Pre-DANA	Post-DANA	Difference pre and post (%)
	% of surface cover by iron oxides			% of surface cover by hydroxyl minerals		
Scrubland	15.52	55.40	**38.88**	**99.25**	**99.48**	**0.23**
Timber pine forest	8.24	46.18	**37.94**	90	95	**5**
Non-irrigated agriculture	54.21	**87.8**	**33.59**	81.91	96.59	**14.68**
Non-irrigated orchards	40.71	59.28	**18.57**	**97.86**	98.57	**0.71**
Non-productive	27.35	45.83	**18.48**	97.23	91.17	**−6.06**
Irrigated citric orchards	**73.25**	**81.58**	**8.33**	95.18	96.49	**1.31**
Irrigated agriculture	**75.35**	**82.47**	**7.11**	53.01	67.39	**14.38**
Grassland	47.58	50.8	**3.22**	95.22	**99.09**	**3.87**
Dry drainage network	**59.98**	52.41	**−7.57**	**99.96**	**100**	**0.04**

As a result, these mineralogical processes have relocated large volumes of contaminated sediments from the headwater mine wastes located on the rambla's headwater to the nearby coastal lagoon *Mar Menor,* where the rambla finally flows. Although it is not the place where erosional processes occur, this natural area is highly affected by the consequences of soil contamination (Boardman et al., 2019). This is due to the contact between the acid runoff water (pH 2–4) of the *rambla* and the alkaline (pH 8) water of the *Mar Menor*, which causes the transported metals to precipitate in the near-shore areas (García & Muñoz-Vera, 2015). In these coastal transition areas like Lo Poyo saltmarsh, polyhydratated sulphates are precipitated as salt efflorescence due to the evaporation of acid mine waters. Efflorescence has a very variable mineralogical composition including natrojarosite ($NaFe_3(SO_4)_2(OH)_6$) or natroalunite ($NaAl_3(SO_4)_2(OH)_6$) (Pérez-Sirvent et al., 2016). This accumulation is also controlled by metals transported as suspended sediments, which reach a greater distance into the lagoon before precipitating (García & Muñoz-Vera, 2015). These deposition processes are translated into a faster clogging of this confined costal lagoon and into a bioavailability of contaminants in the lagoon sediments which has led to the entry of metals into the food chain through the benthic communities (García-Lorenzo et al., 2012; Mountouris et al., 2002).

5.2 | Spectral analysis for mineral identification: Limitations and new perspective

The proposed methodology has reached quite accurate results by a combination of multiple remote sensing techniques. It was possible to map iron oxides and hydroxyl-bearing minerals, validated with results provided by field analyses carried out by Robles-Arenas (2007), Pérez et al. (2013) and Belmonte et al. (2017) in the area, with the consistent distribution of our results over different landforms, and with preliminary results obtained through laboratory reflectance spectroscopy. The results reveal that the proposed approach can capture the mineralogy sedimentary pattern in a semiarid region such as *Sierra Minera de Cartagena*. This suggest that the proposed methodology can be considered as a feasible method to map mining waste processes in other semiarid regions. However, each of the remote sensing techniques applied has its own limitations. For instance, the choice of the break thresholds in the band ratios were derived from a literature review, which can generate uncertain results (Cramer et al., 2021; Sabins, 1999). Also, band ratios only allow a relative quantification of the iron oxides and hydroxyl-bearing minerals. Secondly, in the SAM classification, the strict threshold chosen might generate an underestimation of the affected surface (Shahriari et al., 2014). Finally, the colour composition depends on a subjective visual interpretation, and, therefore, is not suitable for a cross-check with the soil land uses map (Cramer et al., 2021; Sabins, 1999), so it should be cautiously taken into consideration.

In this study, the results obtained with the SAM classification (Figure 9) identified deposits of haematite, goethite, and jarosite. Although the spectral curves are similar, they display different absorption features due to the use of Sentinel-2 MSI red edge bands (B5, B6, B7), narrow NIR band (8A), and atmospheric correction bands (B9). These bands, although spatially inconsistent

and initially designed for vegetation monitoring and atmospheric corrections (European Space Agency, 2015), have been proven to be capable of mapping different iron-bearing minerals. So, as shown by Ge et al. (2020), Lanfranchi et al. (2021) and Soydan et al. (2021), if Sentinel-2 bands are resampled into a uniform spatial resolution, the MSI sensor can be employed to accurately map secondary iron oxides. Also, the possibility to collect cloud-free detailed images close in time (both before and after) to the torrential event has been essential to identify short-term evolution forms of iron oxides, such as jarosite, which reflect environmental acidification processes. This classification has been validated with soil analysis extracted from literature data (Belmonte et al., 2017; Pérez et al., 2013; Robles-Arenas, 2007); out of the 13 available soil samples, 12 points were correctly classified and 1 soil sample was unclassified. Furthermore, the confusion matrix showed an overall accuracy of 87.33%. However, it was not possible to identify different hydroxyl-bearing minerals, as their main absorption and reflection features are located in the SWIR. In this wavelength range, Sentinel-2 sensor only has two bands (B11 and B12), which are not enough to characterise minerals individually.

This paper has presented a classical approach using remote sensing techniques to assess iron oxides and hydroxyl-bearing mineral related to sedimentary processes. However, the proposed methodology could be designed as an automatic process. This new automatic approach would enable a continuous, systematic, and almost real-time monitoring routing by producing medium resolutions maps every 5 days. Such automatic tools can, therefore, be used by local authorities to have better knowledge of the contamination levels, especially when a torrential rainfall event has occurred.

6 | CONCLUSIONS

The proposed approach has shown its effectiveness after demonstrating that all the results correlate among them and provide complementary information on the characterisation and the quantification of the studied minerals. There is a clear mineralogical pattern between the flood dynamic and the sediments distribution. On the one hand, hydroxyl-bearing minerals are associated with depressed areas where water is accumulated forming ponds of variable size. On the other hand, iron oxides are located in sedimentary areas where agricultural lands are located, such as agriculture floodplains, where oxidation processes occur more rapidly.

The SAM classification results also confirmed the presence of secondary mineralization processes, as the technique allowed differentiation between deposits from haematite, goethite, and jarosite, which it is a clear advantage in preliminary soil erosion studies linked to contamination.

Furthermore, Sentinel-2 images have shown their capability to study short-term and variable mineral evolution and distribution, due to the possibility to collect detailed data before and after the torrential events. At the same time, the methodology has shown that these images provide accessible, accurate, and inexpensive data for iron and secondary oxidation precipitate minerals mapping.

All these advantages show the suitability of the method to monitor mining waste sedimentation, both in Sierra Minera de Cartagena or in other semiarid contaminated mining areas. However, further research on the quantification of sedimentary volume and mineral composition of sediments is necessary to achieve the potential application of the method in future torrential events. Moreover, the results derived from the image spectral analysis in this research will be complemented with further laboratory analysis in order to reinforce the method and the interpretation for soil contamination zoning for soil remediation and control measures to be implemented more effectively and efficiently.

AUTHOR CONTRIBUTIONS

Inés Pereira: Investigation; formal analysis; writing – original draft; methodology. **Sara Alcalde-Aparicio:** Conceptualization; writing – review and editing. **Montserrat Ferrer-Julià:** Conceptualization; methodology; writing – review and editing. **María Francisca Carreño:** Writing – review and editing. **Eduardo García-Meléndez:** Conceptualization; writing – review and editing; supervision; funding acquisition; methodology.

ACKNOWLEDGEMENTS

Research supported by FEDER/Spanish Ministry of Science and Innovation-Agencia Estatal de Investigación research project ISGEOMIN - ESP2017-89045-R, and HYPOPROCKS (PDC2021-121352-100) by MCIN/AEI/10.13039/501100011033 and the European Union "NextGenerationEU"/PRTR. Inés Pereira obtained a grant from the "Realización de estudios de doctorado en el marco del programa propio de investigación de la Universidad de León" program, financed by "Universidad de León y Programa ULe-Santander".

CONFLICT OF INTEREST

No potential conflict of interest was reported by the author(s).

DATA AVAILABILITY STATEMENT

Data sharing not applicable to this article as no datasets were generated or analysed during the current study.

ORCID

Inés Pereira https://orcid.org/0000-0002-7328-4791
Sara Alcalde-Aparicio https://orcid.org/0000-0002-9184-5214
Montserrat Ferrer-Julià https://orcid.org/0000-0001-8021-1040
María Francisca Carreño https://orcid.org/0000-0003-2536-2852
Eduardo García-Meléndez https://orcid.org/0000-0001-8217-8205

REFERENCES

Adiri, Z., Lhissou, R., El-Harti, A., Jellouli, A., & Chakouri, R. (2020). Recent advances in the use of public domain satellite imagery for mineral exploration: A review of Landsat-8 and Sentinel-2 applications. *Ore Geology Reviews*, *117*, 103–332.

Agencia Estatal de Meteorología (AEMET). (2019). Avance climatológico mensual septiembre 2019 en la Región de Murcia. Available from: http://www.aemet.es/documentos/es/serviciosclimaticos/vigilancia_clima/resumenes_climat/ccaa/region-de-murcia/avance_climat_mur_sep_2019.pdf

Anawar, H. M. (2013). Impact of climate change on acid mine drainage generation and contaminant transport in water ecosystems of semi-arid and arid mining areas. *Physics and Chemistry of the Earth*, *58*, 13–21.

Archarya, B. S., & Kharel, G. (2020). Acid mine drainage from coal mining in the United States- an overview. *Journal of Hydrology*, *588*, 125061.

Azizi, K., Ayoubi, S., Nabiollahi, K., Garosi, Y., & Gislum, R. (2022). Predicting heavy metal contents by applying machine learning approaches and environmental covariates in west of Iran. *Journal of Geochemical Exploration*, *233*, 106921.

Banguira, T., Alfieri, S. M., Menenti, M., & van Niekerk, A. (2019). Comparing thresholding with machine learning classifiers for mapping complex water. *Remote Sensing*, *11*(11), 1–21.

Belmonte, F., Rojo López, S., Romero Díaz, A., Moreno Brotons, J., & Alonso Sarría, F. (2017). Contaminación de suelos por metales pesados en la sierra minera de Cartagena-La Unión y su entorno (Sureste de España). *Geography, Environmental Science*, *51*(52), 171–174.

Blanco-Bernardeau, A. (2015). *Estudio de la Distribución Espacial y Cartografía Digital de Algunas Propiedades Físicas, Químicas e Hidrodinámicas de Suelos de la Cuenca del Segura*. [thesis]. Universidad Politécnica de Cartagena.

Boardman, J., Vandaele, K., Evans, R., & Foster, I. D. L. (2019). Off-site impacts of soil erosion and runoff: Why connectivity is more important than erosion rates. *Soil Use and Management*, *35*, 245–256.

Brodu, N. (2017). Super-resolving multiresolution images with band-independent geometry of multispectral pixels. *IEEE Transactions on Geoscience and Remote Sensing*, *55*(8), 4610–4617.

Buzzi, J., Riaza, A., García-Meléndez, E., Carrère, V., & Holzwarth, S. (2016). Monitoring of river contamination derived from acid mine drainage using airborne imaging spectroscopy (HyMap data, south-West Spain). *River Research and Applications*, *32*, 125–136.

Byrne, P., Wood, P. J., & Reid, I. (2012). The Impairement of river systems by metal mine contamination: A review including remediation options. *Critical Reviews in Enviornmental Science and Technology*, *42*, 2017–2077.

Cardoso-Fernandes, J., Lima, A., & Teodoro, A. C. (2018). Potential of Sentinel-2 data in the detection of lithium (Li)-bearing pegmatites: A study case. *Earth Resources and Environmental Remote Sensing/GIS Applications IX*, *10790*, 201–215.

Chen, F., Van de Voorde, T., Roberts, D., Zhao, H., & Chen, J. (2021). Detection of ground materials using normalized difference indices with a threshold: Risk and ways to improve. *Remote Sensing*, *13*, 1–9.

Cramer, A. S., Calvin, W. M., McCoy, S. W., Breitmeyer, R. J., Haagsma, M., & Kratt, C. (2021). Mapping potentially acid generating material on abandoned mine lands using remotely piloted aerial systems. *Minerals*, *11*(4), 365.

Creeper, N., Fitzpatrick, R., & Shand, P. (2012). The occurrence of inland acid sulphate soils in the floodplain wetlands of the Murray–Darling basin, Australia, identified using a simplified incubation method. *Soil Use and Management*, *29*, 130–139.

de Sousa Mendes, W., Demattê, J. A. M., de Resende, M. E. B., Chimelo Ruiz, L. F., de Mello, D. C., Tadeu Fim Rosas, J., Quiñonez Silvero, N. E., Ferracciú Alleoni, L. R., Colzato, M., Rosin, N. A., & Rabelo Campos, L. (2022). A remote sensing framework to map potential toxic elements in agricultural soils in the humid tropics. *Environmental Pollution*, *292*, 118397.

Diedhiou, S., Goudiaby, A. O. K., Sagna, Y. P., Diatta, Y., Diallo, M. D., & Ndoye, I. (2020). Effect of iron toxicity on rice growth in Sulfato-ferruginous lowland of South Senegal. *American Journal of Agriculture and Forestry*, *8*(1), 9–14.

Du, Y., Zhang, Y., Ling, F., Wang, Q., Li, W., & Li, X. (2016). Water bodies' mapping from sentinel-2 imagery with modified normalized difference water index at 10-m spatial resolution produced by sharpening the SWIR band. *Remote Sensing*, *8*(4), 1–19.

Elberling, B., Breuning-madsen, H., Hinge, H., & Asmud, G. (2010). Heavy metals in 3300-year-old agricultural soils used to assess present soil contamination. *European Journal of Soil Science*, *61*, 74–83.

European Space Agency. (2015). User Guides - Sentinel-2 MSI - Sentinel Online - Sentinel Online. Available from: https://sentinel.esa.int/web/sentinel/user-guides/sentinel-2-msi

European Space Agency. (2018). Sentinel-2 toolbox. Available from: https://sentinel.esa.int/web/sentinel/toolboxes/sentinel-2. Source code: https://github.com/senbox-org/s2tbx

European Space Agency. (2019). GMES Sentinel-2 Mission Requirements Document; Technical Report Issue 2 Revision. Available from: http://esamultimedia.esa.int/docs/GMES/Sentinel-2_MRD.pdf

Fan, R., Quian, G., Li, Y., Short, D. M., Schumann, C. R., Chen, M., Smart St, R., & Gerson, A. R. (2022). Evolution of pyrite oxidation from a 10-year kinetic leach study: Implications for secondary mineralisation in acid mine drainage control. *Chemical Geology*, *588*, 120653.

FAO-WRB. (2007). *World Reference Base for soil resources*. ISRIC, ISSS Press, Rome, Italy.

Fernández-Naranjo, F. J., Arranz-González, J. C., Rodríguez-Gómez, V., Rodríguez-Pacheco, R., & Vadillo, L. (2020). Geochemical anomalies for the determination of surface stream

sediments pollution: Case of Sierra de Cartagena-La Unión mining district, Spain. *Enviornmental Monitoring and Assessment*, *192*, 247.

Franto, S. P., & Donny, L. (2018). Alteration mineral mapping to identify primary tin potential using Landsat 8 images and geographic information system in Rimba Kulit Area, Southern of Bangka Island. *Earth Science, Mineral, and Energy*, *212*, 012021. https://doi.org/10.1088/1755-1315/212/1/012021

García, C. (2004). *Impacto y riesgo ambiental de los residuos minero-metalúrgicos de la Sierra de Cartagena-La Unión (Murcia-España)* [thesis]. Universidad Politécnica de Cartagena.

García, G., & Muñoz-Vera, A. (2015). Characterization and evolution of the sediments of a Mediterranean coastal lagoon located next to a former mining area. *Marine Pollution Bulletin*, *100*, 249–263.

García-Lorenzo, M. L., Pérez-Sirvent, C., Martínez-Sánchez, M. J., & Molina-Ruiz, J. (2012). Trace elements contamination in an abandoned mining site in a semiarid zone. *Journal of Geochemical Exploration*, *113*, 23–35.

Ge, W., Cheng, Q., Jing, L., Wang, F., Zhao, M., & Ding, H. (2020). Assessment of the capability of sentinel-2 imagery for iron-bearing minerals mapping: A case study in the cuprite area. *Nevada. Remote Sensing*, *12*(18), 1–16.

Githenya, L. K., Kariuki, P. C., & Waswa, A. K. (2019). Application of remote sensing in mapping hydrothermal alteration zones and geological structures as areas of economic mineralization in Mwitika-Makongo Area, SE Kenya. *Journal of Environment and Earth Science*, *9*(11), 16–27. https://doi.org/10.7176/JEES/9-11-03

Grealish, G. J., & Fitzpatrick, R. W. (2013). Acid sulphate soil characterization in Negara Brunei Darussalam: A case study to inform management decisions. *Soil Use and Management*, *29*(3), 432–444.

Hua, L., Man, W., Wag, Q., & Zhao, X. (2012). A new decision tree classification approach for extracting urban land from Landsat TM in a Coastal City, China. In B. Werned (Ed.), *Fourth international symposium on information science and engineering; December 14–16, 2012* (pp. 282–286). Shanghai.

Jordán-Vidal, M. M., Montero-Martínez, M. A., García-Sánchez, E., & Martinez-Poveda, A. (2020). Metal contamination of agricultural soils amended with biosolids (sewage sludge) at a ceramic production area in NE Spain: A 10-year resampling period. *Soil Use and Management*, *37*(2), 307–318.

Karimi, M., Sedighi, A., Kiavarz, M., Qureshi, S., Haase, D., & Alavipanah, K. (2019). Automated built-up extraction index: A new technique for mapping surface built-up areas using LANDSAT 8 OLI imagery. *Remote Sensing*, *11*(17), 1–20.

Kariuki, P. C., & Van der Meer, F. D. (2003). Swelling Clay Mapping for characterizing expansive soils; results from laoratory spectroscopy and Hysens DAIS analysis. In M. Habermeyer, A. Muellller, & S. Holzwarth (Eds.), *3rd EARSeL workshop on imaging spectroscopy; May 13–16, 2003; Oberpfaffenhofen* (pp. 220–235). BIS Verlag.

Kicińska, A., Pomykała, R., & Izquierdo-Diaz, M. (2021). Changes in soil pH and mobility of heavy metals in contaminated soils. *European Journal of Soil Science*, *73*, e13203.

Koch, M. (2000). Geological controls of land degradation as detected by remote sensing: A case study in Los Monegros, north-East Spain. *International Journal of Remote Sensing*, *21*(3), 457–473.

Kruse, F. A., Lefkoff, A. B., Boardman, J. W., Heidebrecht, K. B., Shapiro, A. T., Barloon, P. J., & Goetz, A. F. H. (1993). The spectral image processing system (SIPS)-interactive visualization and analysis of imaging spectrometer data. *Remote Sensing Environment*, *4*, 145–163.

Lanfranchi, R. A., Cerqueira, P. C. S., & Rocha, F. (2021). Application of remote sensing and reflectance spectroscopy to explore iron-enriched domains in the north region of the intracontinental sector of the Aracuai West Congo Orogen. *Ore Geology Reviews*, *128*, 103916.

López-García, J. A., Lunar, R., & Oyarzun, R. (1988). Silver and lead mineralogy in Gossan-type deposits of Sierra de Cartagena, Southeast Spain. *Trans Institution of Mining and Metallurgy, Section B*, *97*, 82–88.

Martín-Crespo, T., Gómez-Ortiz, D., Martín-Velázquez, S., Martínez-Pagán, P., Ignacio-San José, C., Lillo, J., & Faz, A. (2020). Abandoned mine tailings affecting riverbed sediments in the Cartagena–La Union District, Mediterranean Coastal Area (Spain). *Remote Sensing*, *12*(12), 2042.

Martín-Vide, J., Moreno-García, M. C., & López-Bustins, J. (2021). Synoptic causes of torrential rainfall in South-Eastern Spain (1941-2017). *Geographical Research Letters*, *47*(1), 143–162.

Masoumi, F., Eslamkish, T., Honarmand, M., & Abkar, A. A. (2017). Utilization of aster data and spectral analysis to discriminate hydrothermally altered areas over rabor, South of Kerman. *Iran. Journal of the Indian Society of Remote Sensing*, *45*(6), 1039–1055.

McFeeters, S. K. (1996). The use of the Normalized Difference Water Index (NDWI) in the delineation of open water features. *International Journal of Remote Sensing*, *17*(7), 1425–1432.

Mielke, C., Boesche, N., Rogass, C., Kaufmann, H., Gauert, C., & de Wit, M. (2014). Spaceborne mine waste mineralogy monitoring in South Africa, applications for modern push-broom missions: Hyperion/OLI and EnMAP/Sentinel-2. *Remote Sensing*, *6*(8), 6790–6816.

Ministry of finance and civil service. (2022). Sede Electrónica del Catastro. Available from: https://www.sedecatastro.gob.es/

Ministry of Transport Mobility and Urban Agenda (MITMA). (2017). Sistema de Información de Ocupación del Suelo en España (SIOSE). Available from: https://www.siose.es/web/guest/siose

Mountouris, A., Voutsas, E., & Tassios, D. (2002). Bioconcentration of heavy metals in aquatic environments: The importance of bioavailability. *Marine Pollution Bulletin*, *44*, 1136–1141.

Pan, Y., Fu, Y., Liu, S., Ma, T., Tao, X., Ma, Y., Fan, S., Dang, Z., & Lu, G. (2022). Spatial and temporal variations of metal fractions in paddy soil flooding with acid mine drainage. *Environmental Research*, *212*, 113241.

Panagos, P., Ballabio, C., Poesen, J., Lugato, E., Scarpa, L., Montanarella, L., & Borrelli, P. (2020). A soil erosion indicator for supporting agricultural, environmental and climate policies in the European Union. *Remote Sensing*, *12*, 1365.

Panagos, P., Borrelli, P., Poesen, J., Ballabio, C., Lugato, E., Meusburgerv, K., Montanerella, L., & Alewell, C. (2015). The new assessment of soil loss by water erosion in Europe. *Environmental Science and Policy*, *54*, 438–447.

Pellegrini, S., García, G., Peñas-Castejón, J. M., Vignozzi, N., & Costantini, E. A. C. (2016). Pedogenesis in mine tails affects macroporosity, hydrological properties, and pollutant flow. *Catena*, *136*, 3–16.

Pereira, I. (2020). *Análisis espectral de óxidos de hierro mediante imágenes satelitales del sentinel 2 [project]*. Universidad de León.

Pérez, C., Martínez-Sánchez, M. J., & Martínez-López, S. (2013). Mineralógica de los Suelos, Indicador para la delimitación de las Zonas de Influencia Minera. *Macla*, *17*, 87–88.

Pérez-Sirvent, C., Hernández-Pérez, C., Martínez-Sánchez, M. J., García-Lorenzo, M. L., & Bech, J. (2016). Geochemical characterisation of surface waters, topsoils and efflorescences in a historic metal-mining area in Spain. *Journal of Soils and Sediments*, *16*, 1238–1252.

Ramírez, I., Vicente, M., García, J. A., & Vaquero, A. (1999). *Mapa Digital de Suelos de la Región de Murcia*. Consejería de Agricultura, Agua y Medio Ambiente.

Ranghetti, L., Boschetti, M., Nutini, F., & Busetto, L. (2020). sen2r: An R toolbox for automatically downloading and preprocessing Sentinel-2 satellite data. *Computers & Geosciences*, *139*, 104473. Available from: https://sen2r.ranghetti.info

Rasheed, A., Hassan, M. U., Aamer, M., Brian, J. M., Xu, Z. R., He, X. F., Yan, G., & Wu, Z. M. (2020). Iron toxicity, tolerance and quantitative trait loci mapping rice; a review. *Applied Ecology and Environmental Research*, *18*(6), 7483–7498.

Riaza, A., Buzzi, J., García-Meléndez, E., Carrère, V., & Müller, A. (2011). Monitoring the extent of contamination from acid mine drainage in the Iberian Pyrite Belt (SW Spain) using hyperspectral imagery. *Remote Sensing*, *3*(10), 2166–2186.

Richter, N. (2010). *Pedogenic iron oxide determination of soil surfaces from laboratory spectroscopy and HyMap image data. A case study in Cabo de Gata-Níjar Natural Park, SE Spain*. [thesis]. Humboldt Universität.

Richter, R., Louis, J., & Müller-Wilm, U. (2012). Algorithm Sentinel-2 MSI – Level 2A Products Algorithm Theoretical Basis Documents. S2PAD-ATBD-0001, Issue 2.0.

Robles-Arenas, V. M. (2007). *Caracterización hidrogeológica de la Sierra de Cartagena-La Unión (SE de la Península Ibérica). Impacto de la minería abandonada sobre el medio hídrico* [thesis]. Universidad Politécnica de Cataluña.

Robles-Arenas, V. M., Rodríguez, R., García, C., Manteca, J. I., & Candela, L. (2006). Sulphide-mining impacts in the physical environment: Sierra de Cartagena–La Unión (SE Spain) case study. *Envionmental Geology*, *51*, 47–64.

Rowan, L. C., & Mars, J. C. (2003). Lithologic mapping in the mountain pass, California area using Advanced Spaceborne Thermal Emission and Reflection Radiometer (ASTER) data. *Remote Sensing of Environment*, *84*, 350–366.

Rowan, L. C., Mars, J. C., & Simpson, C. J. (2005). Lithologic mapping of the Mordor, NT, Australia ultramafic complex by using the Advanced Spaceborne Thermal Emission and Reflection Radiometer (ASTER). *Remote Sensing of Environment*, *99*(1–2), 105–126.

Sabins, F. F. (1999). Remote sensing for mineral exploration. *Ore Geolgy Reviews*, *14*, 157–183.

Sahwan, W., Lucke, B., Sprafke, T., Vanselow, K. A., & Bäumler, R. (2020). Relationships between spectral features, iron oxides and colours of surface soils in northern Jordan. *European Journal of Soil Science*, *72*, 80–97.

Sanz de Galdeano, C. (1990). Geologic evolution of the Betic Cordilleras in Western Mediterranean. *Miocene to the present. Tectonophysics*, *172*(1–2), 107–119.

Shahriari, H., Ranjbar, M., Honarmand, E., & Carranza, J. M. (2014). Selection of less biased threshold angles for SAM classification using the real value–area fractal technique. *Resource Geology*, *64*(4), 301–315.

Shi, X. Z., Oldmeadow, D., & Aspandiar, M. (2015). Observations on mineral transformations and potential environmental consequences during the oxidation of ironsulphide-rich materials in incubation experiments. *European Journal of Soil Science*, *66*, 393–405.

Singhal, R. K., Kumar, M., Bose, B., Mondal, S., Srivastava, S., Dhankher, O. P., & Tripathi, R. D. (2022). Heavy metal (loid)s phytotoxicity in crops and its mitigation through seed priming technology. *International Journal of Phytoremediation*, *13*, 1–20.

Soydan, H., Koz, A., & Şebnem Düzgün, H. (2021). Secondary iron mineral detection via hyperspectral unmixing analysis with sentinel-2 imagery. *International Journal of Applied Earth Observation and Geoinformation*, *101*, 102343.

Torres-Roldán, R. L. (1979). The tectonic subdivision of the Betic zone (Betic Cordilleras, southern Spain): Its significance and one possible geotectonic scenario for the westernmost Alpine belt. *American Journal of Science*, *279*, 19–51.

United States Geological Survey. (2017). Spectral Library. Available from: https://www.usgs.gov/labs/spec-lab/capabilities/spectral-library

Van der Meer, F. D. (2001). Basic physics of spectrometry. In F. D. Van der Meer & S. M. de Jong (Eds.), *Imaging spectrometry: Basic principles and prospective applications (remote sensing and digital image processing; 4)* (pp. 3–16). Kluwer.

Van der Meer, F. D. (2004). Analysis of spectral absorption features in hyperspectral imagery. *International Journal of Applied Earth Observation and Geoinformation*, *5*, 55–68.

Van Der Meer, F. D., Van der Werff, H. M. A., Van Ruitenbeek, F. J. A., Hecker, C. A., Bakker, W. H., Noomen, M. F., Van der Meijde, M., Carranza, E. J. M., de Smeth, J. B., & Woldai, T. (2012). Multi- and hyperspectral geologic remote sensing: A review. *International Journal of Applied Earth Observation and Geoinformation*, *14*(1), 112–128.

Velasco, A. M., Pérez-Ruzafa, A., Martínez-Paz, J. M., & Marcos, C. (2017). Ecosystem services and main environmental risks in a coastal lagoon (Mar Menor, Murcia, SE Spain): The public perception. *Journal of Nature Conservation*, *43*, 180–189.

Vijdea, A., Sommer, S., & Mehl, W. (2004). *Use of remote sensing for mapping and evaluation of mining waste anomalies at national to multi-country scale. A case study to integrate remote sensing information with thematic data layers and national inventories on mining features in pre-accession countries*. European Commission.

Xia, L., Bi, R., Song, X., & Lv, C. (2020). Dynamic changes in soil erosion risk and its driving mechanism: A case study in the LoessPlateau of China. *European Journal of Soil Science*, *72*, 1312–1331.

Xu, S., Zhao, Y., Wang, M., & Shi, X. (2022). A comparation of machine learning algorithms for mapping soil iron parameters indicative of pedogenesis processes by hyperspectral imaging of intact soil profiles. *European Journal of Soil Science*, *70*(1), e13204.

Yadav, S. K., Banerjee, A., Jhariya, M. K., Meena, R. S., Khan, N., & Raj, A. (2022). Eco-restoration of bauxite mining: An ecological approach. In M. K. Jhariya, R. S. Meena, A. A. N. D. Banerjee, & S. N. Meena (Eds.), *Natural resources conservation and advances for sustainability*. Elsevier.

Zabic, N., Rivard, B., Ong, C., & Mueller, A. (2014). Using airborne hyperspectral data to characterize the surface pH and mineralogy of pyrite tailings. *International Journal of Applied Earth Observation and Geoinformation*, *32*, 152–162.

Zha, Y., Gao, J., & Ni, S. (2003). Use of normalized difference built-up index in automatically mapping urban areas from TM imagery. *International Journal of Remote Sensing*, *24*(3), 583–594.

Zhang, B., Guo, B., Zou, B., Wei, W., Lei, Y., & Li, T. (2022). Retrieving soil heavy metals concentrations based on GaoFen-5 hyperspectral satellite image at an opencast coal mine, Inner Mongolia, China. *Environmental Pollution*, *300*, 118981.

How to cite this article: Pereira, I., Alcalde-Aparicio, S., Ferrer-Julià, M., Carreño, M. F., & García-Meléndez, E. (2023). Monitoring sedimentary areas from mine waste products with Sentinel-2 satellite images: A case study in the SE of Spain. *European Journal of Soil Science*, *74*(1), e13336. https://doi.org/10.1111/ejss.13336